Design and characterization of receive-only surface coil arrays at 3T with integrated solid high permittivity materials

Ruytenberg, T.; O'Reilly, T.P.; Webb, A.G.

Journal of Magnetic Resonance 311 (2020) 106681

Contents lists available at ScienceDirect

Journal of Magnetic Resonance

journal homepage: www.elsevier.com/locate/jmr

Design and characterization of receive-only surface coil arrays at 3T with integrated solid high permittivity materials

Thomas Ruytenberg *, Thomas P. O'Reilly, Andrew G. Webb

C.J. Gorter Center for High Field MRI, Department of Radiology, Leiden University Medical Center, Leiden, the Netherlands

ARTICLE INFO

Article history:
Received 6 September 2019
Revised 16 December 2019
Accepted 28 December 2019
Available online 29 December 2019

Keywords:
High permittivity material
Coil design
Surface coil
Neck imaging

ABSTRACT

A receive-only surface coil array for 3 Tesla integrating a high-permittivity material (HPM) with a relative permittivity of 660 was designed and constructed and subsequently its performance was evaluated and compared in terms of transmit field efficiency and specific absorption ratio (SAR) during transmission, and signal-to-noise ratio during reception, with a conventional identically-sized surface coil array. Finite-difference time-domain simulations, bench measurements and in-vivo neck imaging on three healthy volunteers were performed using a three-element surface coil array with integrated HPMs placed around the larynx. Simulation results show an increase in local transmit efficiency of the body coil of ~10-15% arising from the presence of the HPM. The receiver efficiency also increased by approximately 15% close to the surface. Phantom experiments confirmed these results. In-vivo scans using identical transmit power resulted in SNR gains throughout the laryngeal area when compared with the conventional surface coil array. In particular specifically around the carotid arteries an average SNR gain of 52% was measured averaged over the three subjects, while in the spine an average of 20% SNR gain was obtained.

1. Introduction

High-permittivity materials (HPMs) have been used in many studies as a method to tailor transmit (B_1^+) and/or receive (B_1^-) field efficiencies and spatial distributions. For very high field (7T) a variety of dielectric materials, ranging from plain water [1] to calcium and barium titanate powders mixed with (deuterated) water [2,3] and solid ceramics [4] with relative permittivities ranging from 78 to 300 have been used either to homogenize the B_1^+ field or to produce local focusing of the B_1^+ field for improved imaging of specific anatomies, such as the temperalmandibular joint and the inner ear [5,6]. The receive sensitivity is also affected by these HPMs, which can manifest as an increased SNR [7,8].

HPMs have also been used at clinical field strengths as 1.5 and 3T, with results showing increased SNR [9] and locally increased B_1^+ fields and reduced SAR [9,10]. By considering both Ampère's law with Maxwell's addition and Faraday's law:

$$\nabla \times \boldsymbol{B} = \mu_0(\boldsymbol{J}_c + \boldsymbol{J}_d) = \mu_0(\boldsymbol{J}_c + j\omega\varepsilon\boldsymbol{E}) \quad (1)$$

$$\nabla \times \boldsymbol{E} = -j\omega\boldsymbol{B} \quad (2)$$

where $|\mathbf{J}_c|$ is the conduction current and $|\mathbf{J}_d|$ the displacement current equal to $|j\omega\varepsilon\mathbf{E}|$ with j the imaginary unit, ω the angular frequency and ε the permittivity, higher permittivities are required at these lower fields [11]. Relative permittivity values of 1000 have been used for imaging the spine at 3T [12], values of 1200 and 3300 at 1.5 and 3T for head imaging [13], and 4500 at 1.5T for wrist imaging [14]. In the last two studies, SNR gains of about 50% were demonstrated in-vivo. Vaidya et al. [15] have shown in a simulation study on ideal current patterns that although ultimate intrinsic SNR [16] is not improved using HPMs, these materials can shift the balance between signal-only optimal current patterns and noise-minimizing dark mode current patterns [17], leading to the demonstrated SNR gains for specific coil arrays.

In all of these previous studies, HPMs have been placed inside commercial coil arrays, which can potentially lead to detuning and alterations in the coupling matrices between the various elements of the array. Additionally, in experimental studies these materials never fully cover the entire coil array, or they are used in combination with volume coils, where the coil is far away from the imaged object and therefore from the HPM.

In this study, therefore, we specifically design surface coil arrays with the HPMs integrated into the structure, covering the entirety of the coil array. Electromagnetic simulations, phantom experiments and in-vivo imaging were performed to evaluate the effect on transmit and receive field efficiencies of a receive-only coil with

* Corresponding author at: LUMC, Dept. of Radiology, C3-Q Albinusdreef 2, 2333ZA Leiden, the Netherlands.
E-mail address: t.ruytenberg@lumc.nl (T. Ruytenberg).

https://doi.org/10.1016/j.jmr.2019.106681
1090-7807/

integrated HPM compared to an identically sized conventional coil without HPM.

2. Methods

2.1. Coil manufacturing and characterization

For coil characterization and comparison purposes, a conventional receive-only surface coil with inner dimensions of 73×60 mm^2, conductor width of 3 mm etched on an FR4 PC board, with four tuning capacitors of 27 pF and a balanced capacitive matching network was constructed, with a second one of identical dimensions incorporating a rectangular dielectric block (lead zirconate titanate, PZT, $70 \times 57 \times 10$ mm^3, ε_r = 660, σ = 0.01 S/m, mass = 210 gr, TRS Technologies, State College, PA, USA) placed in the center of the surface coil (Fig. 1a). The dielectric block had no resonances at the imaging frequency (lowest mode $f_{TE01\delta}$ = 267 MHz). For a rectangular waveguide with perfectly reflecting boundaries, resonant frequencies can be determined using the following equation

$$f_0 = \frac{1}{2\sqrt{\mu_r \varepsilon_r}} \sqrt{\frac{m^2}{a^2} + \frac{n^2}{b^2} + \frac{p^2}{d^2}} = \frac{c}{2} \sqrt{\frac{m^2}{a^2} + \frac{n^2}{b^2} + \frac{p^2}{d^2}} \quad (3)$$

with m, n and p the mode numbers, and a, b, and d the length, width and thickness of the dielectric; μ_r and ε_r are the relative permeability and permittivity, respectively. For very high permittivity materials this would be a good approximation, but to estimate both permittivity and conductivity of the material, electromagnetic finite-difference time-domain simulations were performed. In these simulations a dielectric block was simulated with a weakly-coupled pick-up coil on top. Electric permittivity and conductivity were iteratively changed until agreement with bench measurements was found on both the Q-value and eigenfrequencies. Both coils were tuned and matched to 50 Ohms at 127.8 MHz when placed on a tissue-mimicking phantom (ε_r = 45 and σ = 0.4 S/m). Both coils used could be tuned using a 0–10 pF variable capacitor. For matching, the conventional loop used two 28 pF capacitors and the integrated HPM coil two 20 pF capacitors. For detuning during transmission, passive circuits were implemented using crossed diodes (UMX9989AP, Microsemi, Lowell, MA, USA) and an active circuit was implemented using an LC-trap with PIN-diode (MA4P7441F-1091T, MACOM, Lowell, MA, USA) [18].

For in-vivo imaging, three-element receive-only coil arrays were constructed, one array with HPM and a conventional array without. The design was chosen such that the two outer elements are positioned above the carotid arteries and the middle element above the larynx. Individual elements in the arrays were fitted on a 3D-printed curved holder with a radius of 60 mm and were subsequently decoupled using induced current elimination (ICE) circuits [19]. These circuits consist out of three overlapping loops, two of the neighboring elements, and one of the additional resonator in between these loops. The decoupling was tuned using the middle loop with a 10–20 pF variable capacitor. Tuning and matching of the array was performed while loaded with a phantom (ε_r = 79, σ = 0.5 S/m) such that S11-parameters were less than −18 dB and the ICE decoupling between neighboring elements was lower than −22 dB. Coupling between the two non-neighboring elements was −12 dB for both arrays. Floating common-mode chokes of a bazooka type [20] were placed on every channel of the coils with a measured common mode suppression ratio of 20 dB. For MR measurements, a receive interface box was used with low-impedance (~2 Ohm) pre-amplifiers.

2.2. Electromagnetic simulations

All simulations were performed using CST Microwave Studio 2019 (CST MWS, Darmstadt, Germany).

In order to investigate the receive performances of single coil elements, finite difference time-domain (FDTD) simulations were performed using four discrete ports. Capacitors were simulated at these ports as well as a single port on the short side of the coil containing a capacitive matching circuit combined with a driving port. The coil was placed 15 mm away from a rectangular phantom measuring $300 \times 300 \times 200$ mm^3 with a relative permittivity of 60 and a conductivity of 0.4 S/m. B_1^- fields were subsequently obtained using 1 Watt accepted power. The effects of the HPM on the B_1^+ fields were investigated by simulating the three-element in-vivo array on a cylindrical phantom using the birdcage body coil. Finally the in-vivo array was simulated on a body voxel model (Gustav, CST Voxel Family) to estimate changes in the local SAR and the location and value of the maximum SAR_{10g}.

2.3. Imaging sequences

The 3T quadrature body coil was used for transmission in all experiments and the integrated posterior receive coil in the patient bed was disabled. SNR scans on a phantom were performed using proton-density weighted gradient echo sequences with acquisition voxel size = $1 \times 1 \times 5$ mm^3, acquisition matrix = 400×400, TE/TR = 2.2/2000 ms, flip angle = 20°, duration 606 s. Post processing was performed using raw data to obtain absolute SNR units [21]. Transmit efficiency (B_1^+) maps were acquired on a phantom using the Dual Refocusing Echo Acquisition Mode (DREAM) method [22] with a TR extension of 30 ms and a stimulated echo acquisition mode angle of 60°.

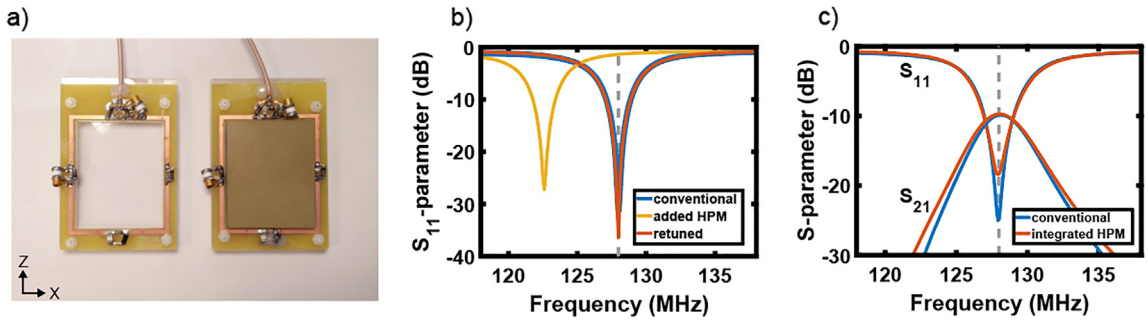

Fig. 1. (a) a photograph of a conventional rectangular surface coil on the left, and on the right a coil with added high permittivity material. (b) S_{11}-parameters of the conventional and integrated HPM coil (before and after retuning). (c) coupling between two conventional coils placed side by side with 45 mm separation, and the corresponding plot for two coils with integrated HPMs.

For all in-vivo scans on healthy volunteers IRB approval for this study was obtained and written informed consent was acquired from every volunteer prior to their participation.

In-vivo, carotid artery imaging was performed using turbo spin echo (TSE) black blood sequences, triggered on the cardiac cycle. T1-weigthed imaging was performed with parameters: acquisition voxel size = 0.55 × 0.75 × 3 mm^3, acquisition matrix = 272 × 198, TE/TR = 9/1333 ms, slices = 9, duration = 288 s and T2-weigthed imaging using acquisition voxel size = 0.55 × 0.75 × 3 mm^3, acquisition matrix = 272 × 195, TE/TR = 80/3750 ms, slices = 9, duration = 210 s. For the SNR measurements, a single-slice T1-weighted black blood sequence was run with the following parameters: acquisition voxel size = 0.55 × 0.75 × 3 mm^3, acquisition matrix = 272 × 198, TE/TR = 9/882 ms, duration = 21 s. The in-vivo coils were used in combination with a radiotherapy head cushion (Black MaxSupports wideshaped, MacroMedics, Waddinxveen, The Netherlands) to reduce head motion during scanning, for subject comfort, and for slightly lifting up the chin for increased accessibility to the neck enabling easier positioning of the coil.

In the experimental comparison of elements and arrays with and without HPM, the following method was adhered to for comparisons when the data was acquired in series. First the coil with HPM was positioned and a full system calibration was initiated including but not limited by an f_0 determination, B_0- and B_1-shimming and a power optimization after which scanning was performed. The coils were interchanged to the coil without HPM and scanning was performed without recalibrating the system. Not recalibrating ensures that no unknown parameters were changed by the system.

3. Results

Fig. 1(a) shows a photograph of the conventional surface coil and one with an integrated HPM block. Fig. 1(b) plots the respective S_{11} parameters when the block is simply placed inside the conventional surface coil. As expected the resonance frequency decreases (by approximately 5 MHz) due to the presence of the material. Notice that the Q-value is essentially unchanged,

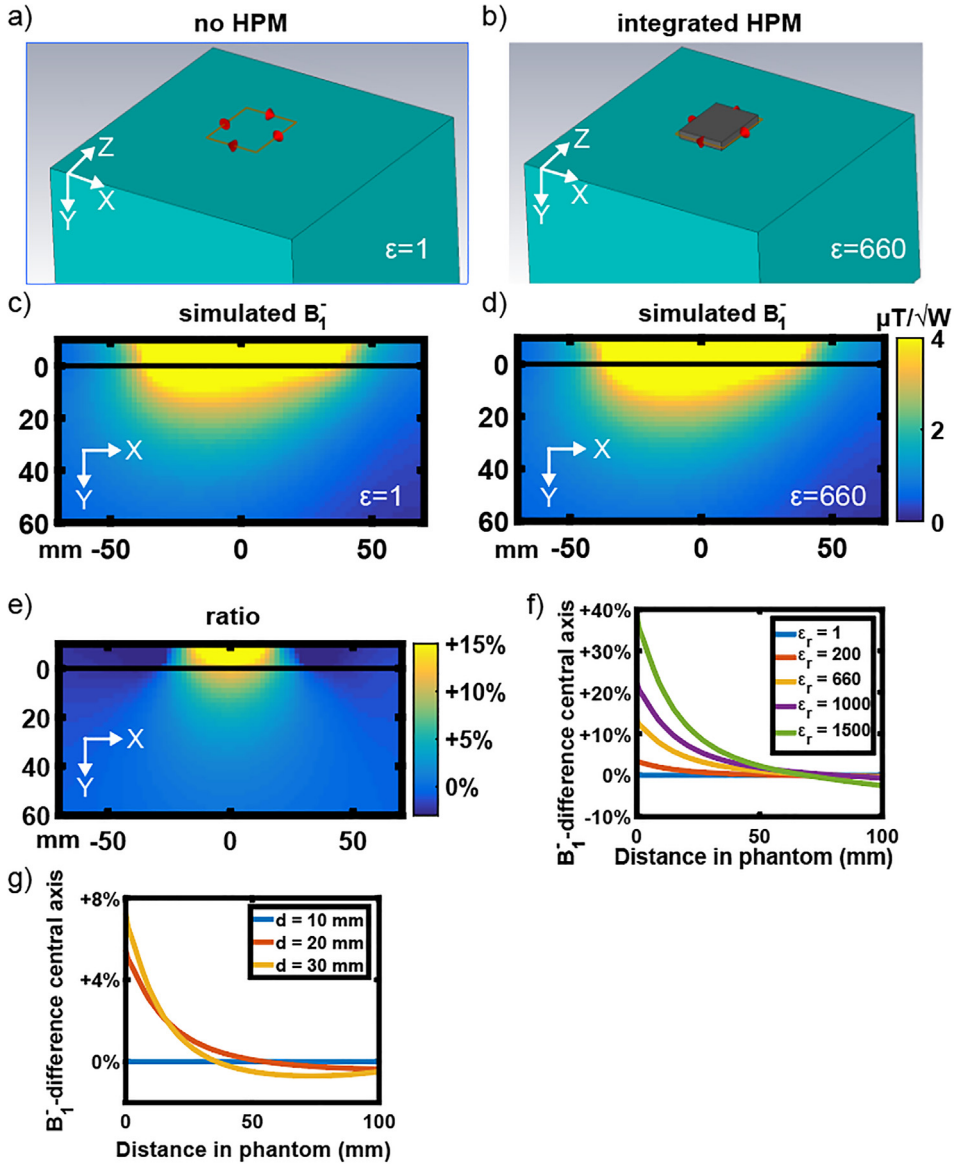

Fig. 2. Simulated B_1^- fields in a phantom. (a) and (c) surface coil with no HPM, (b) and (d) surface coil with HPM ε_r = 660, σ = 0.01 S/m), (e) Ratio of the B_1^- field with HPM relative to that without HPM, showing a maximum of 15% increase, (f) Plot of the ratio along the central axis of the coil as a function of depth in the phantom for different permittivities (constant conductivity of 0.01 S/m). (g) varying thickness of the HPM (ε_r = 660, σ = 0.01 S/m), while the distance from the bottom of the HPM to the phantom is kept constant. All B_1^- simulations were performed using 1 W accepted power.

indicating that the loss tangent of the material is low. The unloaded/loaded Q-values were measured to be 6.5 and 3.3 for elements with and without HPM, respectively. The coil with integrated HPM is simply retuned by adjusting the variable capacitor opposite the matching network. Fig. 1(c) shows the coupling behavior between two loaded coils placed close to one another: the characteristics with and without the HPM are essentially identical.

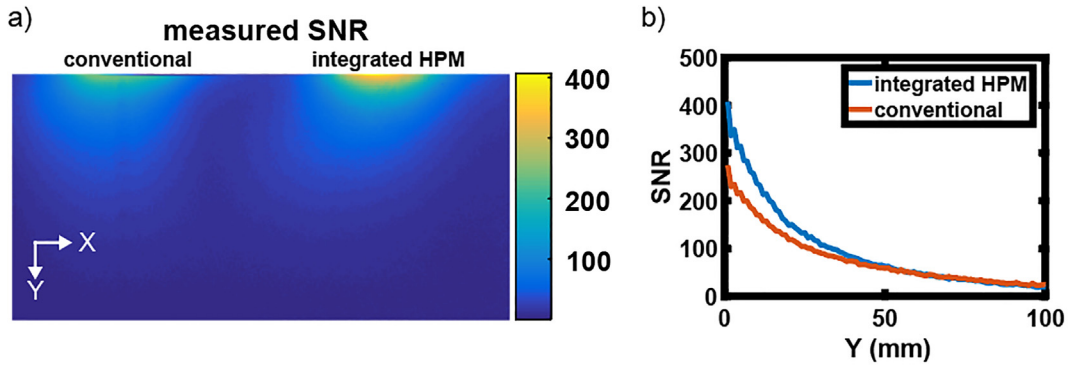

Fig. 3. SNR comparison of a single-element conventional and integrated HPM coil placed on a tissue-mimicking phantom. Setup and axes as in Fig. 1a. (a) Proton-density weighted gradient echo image. (b) SNR plot along the central axis of each coil. Some Gibbs ringing is noticeable in the profiles.

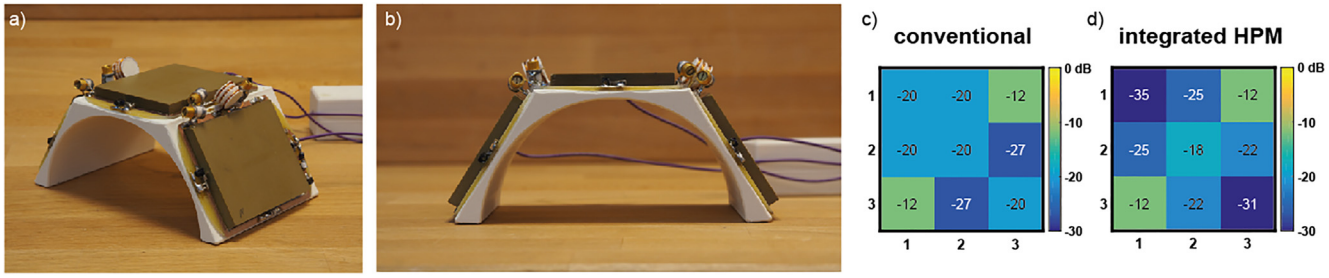

Fig. 4. The three-channel array used for in-vivo measurements with integrated HPM. An identical array was constructed without HPM for comparison (not shown). (a) overview, (b) front view. (c) and (d) show measured S-parameter matrices on a cylindrical phantom.

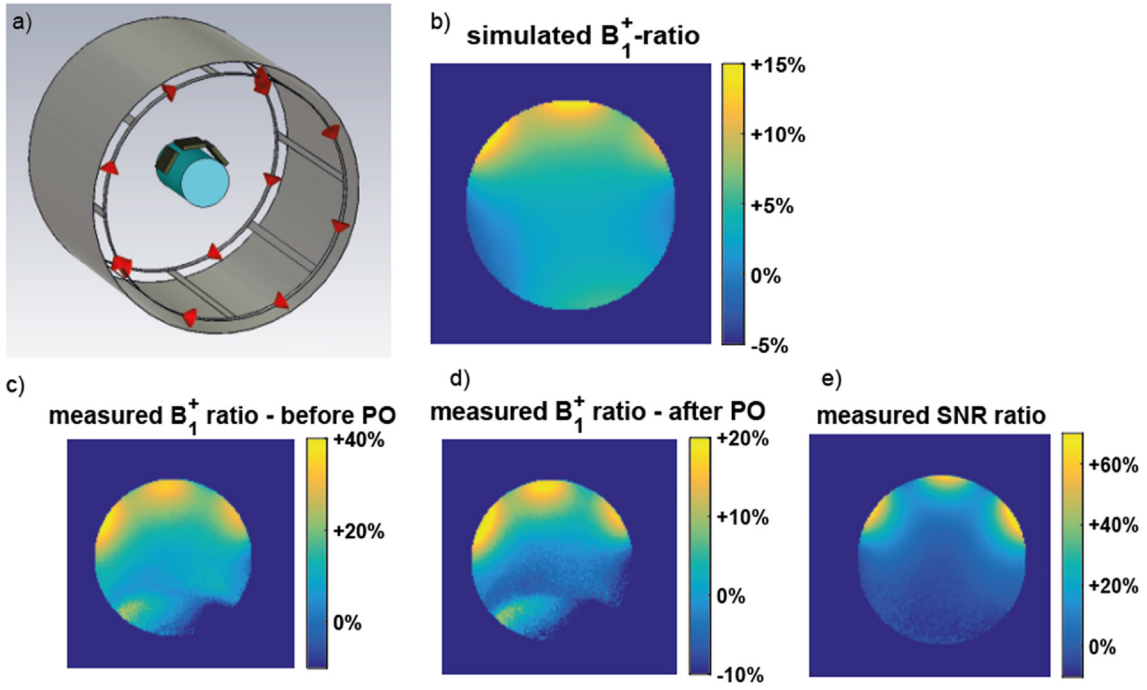

Fig. 5. Simulations and comparative measurements of the B_1^+ fields using the in vivo array. (a) simulation setup, showing the transmit birdcage. (b) the ratio map of two B_1^+ field simulations on a phantom, one with HPM and one without. (c) measured B_1^+ ratio of HPM/noHPM without power optimization (PO). (d) measured B_1^+ ratio of HPM/noHPM with PO. 41% less power was used, resulting in about 20% less B_1^+. (e) measured SNR ratio of HPM/noHPM (after PO). A 60% increase in SNR is measured in the vicinity of the HPM.

Fig. 2(a) shows a graphical representation of the simulation setup for the surface coil without HPM, and Fig. 2(b) the one with the HPM. Corresponding B_1^- maps are shown in Fig. 2(c) and (d) respectively. The ratio of these two maps shows local differences close to the dielectric, as illustrated in Fig. 2(e). Up to a 15% increase in the B_1^- is observed at the surface, with the ratio reducing to unity at a depth of ~80 mm. The B_1^- gains were also studied for different simulated permittivities as shown in Fig. 2(f). Higher permittivities show higher gains at the surface, although these are accompanied by some loss at increasing depths compared to no HPM: for example for the case of $\varepsilon_r = 1500$ the ratio is less than unity for depths greater than ~70 mm. Fig. 2(g) finally shows the effect of using HPM of a different thickness, while keeping the distance between the bottom of the HPM and the phantom constant. Thicker HPM shows higher surface gains, but at depth B_1^- fields are slightly lower.

Fig. 3 shows experimental results comparing the SNR of images acquired with a conventional surface coil and one with the integrated HPM placed on the same phantom. There was a 200 mm distance between the center of the elements to ensure that there was no coupling between them. SNR images are shown in Fig. 3 (a) and a plot of the SNR along the central axis is shown in Fig. 3 (b) for both elements. A 49% increase in SNR at the surface is measured. As these measurements were performed with a low tip angle gradient echo sequence, the measured SNR increase is proportional to the product of the B_1^+ and B_1^- fields. Electromagnetic

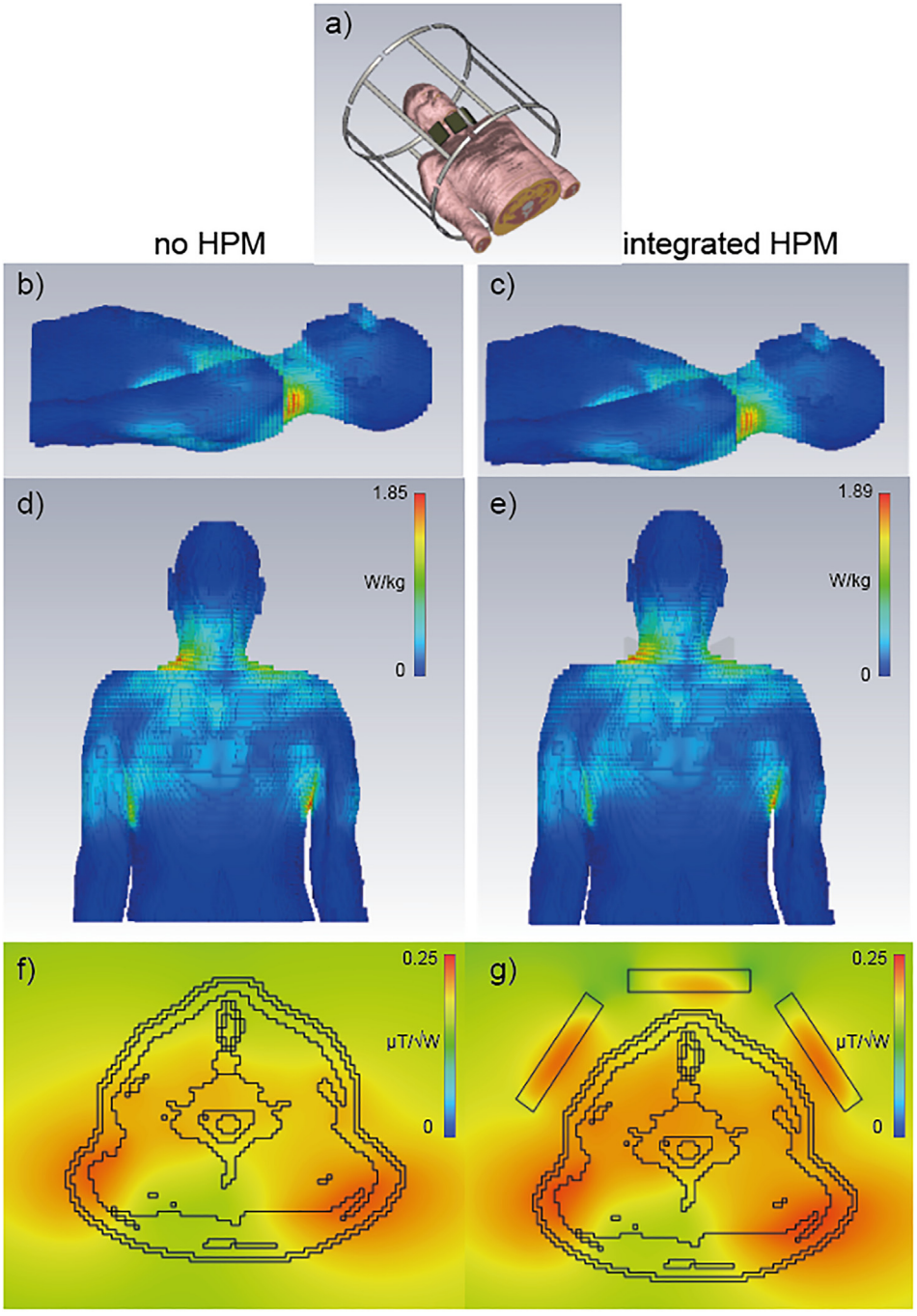

Fig. 6. SAR_{10g} simulations using the body coil on a voxel model (a) simulation setup (birdcage shield not shown for visibility). (b) and (c) side view for no HPM and integrated HPM, showing the location of the maximum SAR on the posterior side of the neck. (d) and (e) posterior view. An increase of 2% maximum SAR_{10g} is observed when using the integrated HPM coil with equal accepted power. (f) and (g) Simulated B_1^+ fields in a transversal slice in the neck.

simulations show that the B_1^+ field from the transmit coil is enhanced by ~15% at the surface by the HPM (see also results in Fig. 5(a). Thus the measured enhancement in the images is somewhat greater than the simulated value of ~32%.

Fig. 4(a) and (b) show photographs of the three coil array with integrated HPMs (an identical setup without HPMs was also constructed). The measured S-parameter matrices are shown in Fig. 4(c) and (d), showing very similar characteristics in terms of inter-element decoupling.

Since it is well-known that HPMs alter the B_1^+ distribution, a simulation was performed using the setup shown in Fig. 5(a). The results are shown in Fig. 5(b) which indicates an increase in the B_1^+ with HPM present of approximately 15% directly below the HPM. Fig. 5(c) shows the experimental results obtained using

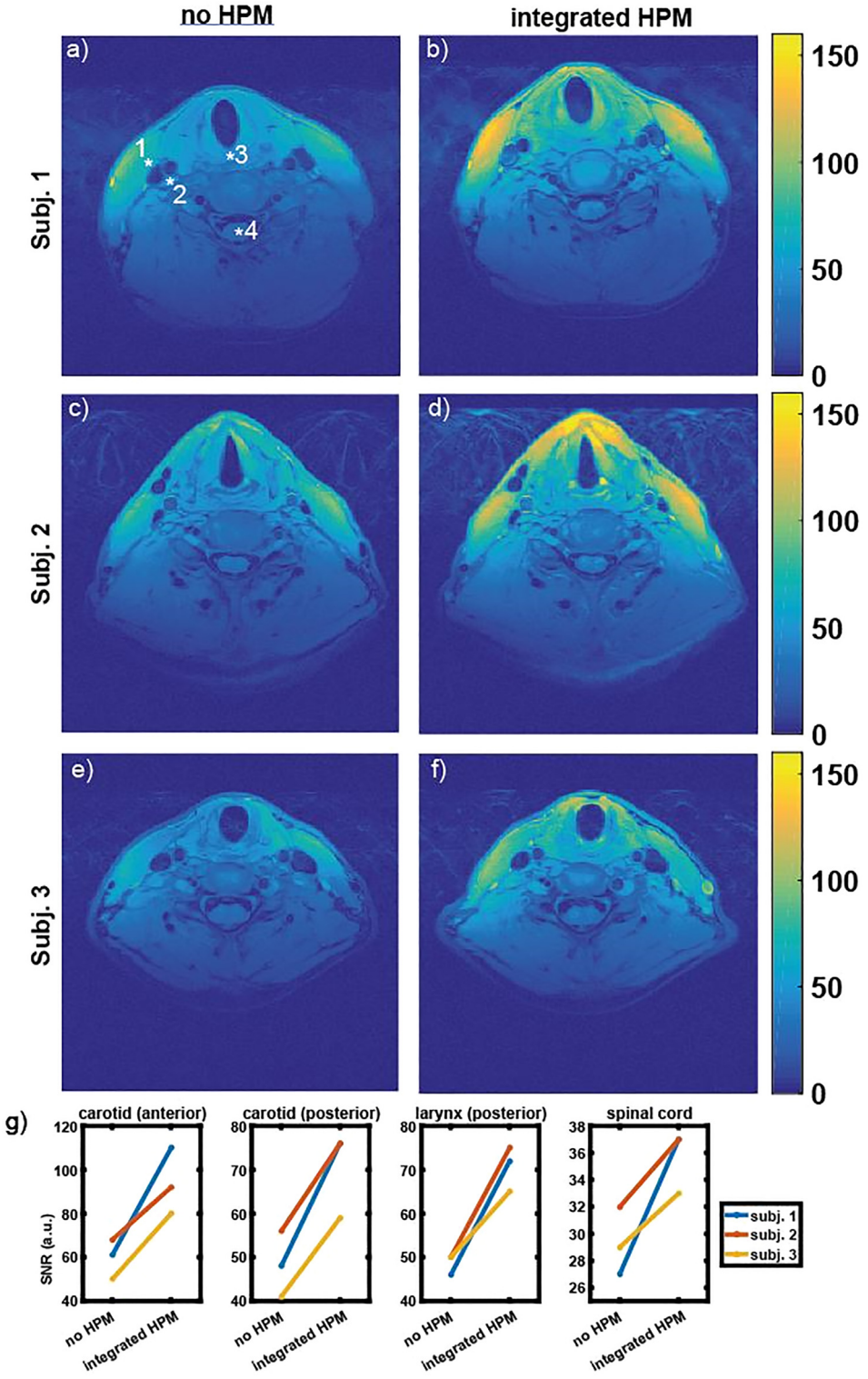

Fig. 7. In-vivo SNR for three subjects using T1-weighted TSE sequences. (a), (c), (e) conventional array. (b), (d), (f) integrated HPM array. For every subject the same transmit power was used between scans with the two arrays. (g) SNR for the conventional and integrated HPM array at the points depicted in Figure (a), measured in the three subjects. For all subjects SNR gains are observed all four points.

the DREAM sequence, which show a slightly higher maximum value of 40% with good co-location of the areas of increased transmit efficiency when compared with the simulation results. Power was not adjusted in the comparison of Fig. 5(c), while for (5d) this optimization was performed. Fig. 5(e) finally shows the SNR ratio of the setup with and without HPM where a power optimization was performed for both setups individually as in Fig. 5(d). A 60% increase in SNR is observed close to the HPM.

Fig. 6 shows SAR and B_1^+ simulations on a voxel body model using the transmit body coil. The neck of the body model was centered in the coil and simulations were run without and with three HPM blocks (ε_r = 660) on the anterior side of the neck corresponding to the three-element coil array. Simulations were run with 1 Watt accepted power and SAR_{10g} was calculated. The figure shows the location of maximum SAR to be on the posterior side of the neck for both simulation without and with HPM present. A 2% increase in the maximum SAR_{10g} from 1.85 W/kg to 1.89 W/kg is observed when applying the HPM. The B_1^+ simulations show a 5–20% B_1^+ increase in the anterior side of the neck.

Fig. 7 shows results from in to vivo scanning of three volunteers using both conventional and integrated HPM coil arrays. The coil covers the anterior part of the neck, and so can be used for either laryngeal imaging [23] or also carotid artery imaging. The SNR was compared at four points: 1. the anterior side of the carotid artery, 2. the posterior side of the carotid artery, 3. the posterior side of the larynx, and additionally a deeper anatomy at point 4, the spinal cord. The same transmit power was applied for both sets of scans. An increase in SNR is observed in all regions for all volunteers when the coil with integrated HPM is used and around the carotid artery specifically, an increase of 52% is measured. The posterior side of the larynx shows an average increase of 45% and for the spinal cord an average increase of 20% is observed. The depth of the center of the spinal cord (point 4 in Fig. 7(a) from the skin surface at the position of the outer coil elements was measured to be 61, 52, and 55 mm for the three subjects. That SNR gains are achieved at these depths can possibly be explained by both the semiannular geometry causing all elements to contribute to the signal at this point, and by the air cavity of the throat, possibly leading to a slightly higher penetration depth than simulated on the uniform phantoms. Supplementary Fig. S1 shows an animation of a 3D time-of-flight sequence where the full carotid arteries were imaged using the integrated HPM coil.

4. Conclusion and discussion

The results presented here show that by specifically designing receive-only surface coil arrays with integrated HPMs both the local transmit and receive efficiencies can be increased by 15 to 20% close to the surface with only a very small (~2%) increase in SAR. SNR gains of up to 52% averaged over three subjects were measured in vivo. The implemented ICE decoupling circuits allowed for additional freedom in array design compared to overlapping elements, as in the case of overlapping, the amount of overlap will be slightly different when integrating HPM and therefore result in a slightly different coverage.

For the in vivo scans the choice was made to compare coils with and without integrated HPM using the same transmit power to study the SNR differences. In general, literature shows that using HPM introduces B_1^+ gains which can be compensated by using less transmit power [9,12,24]. Not using equal power in this study would therefore lead to lower transmit power for the coil with integrated HPM and subsequently a lower SAR than simulated. The influence of recalibrating the utilized power was assessed during phantom scans in Fig. 5, showing that 41% less power for the HPM coil can be used compared to the conventional coil when requesting a 90° flip angle in the isocenter transversal plane. We anticipate that this difference in power can also be achieved during the in vivo scans and that due to not applying this optimization when switching to the conventional coil, the achieved flip angles for the no HPM case in Fig. 7 might have been slightly lower than requested.

While central axis gains are evident from Fig. 2, a lower field-of-view is also observed in the figure, as the ratio in Fig. 2e is slightly below unity at about 50 mm from the central axis in the X-direction. This is also the case Z-direction (not shown). The reduced field-of-view in the X-direction is compensated for in the in-vivo array due to its semi-annual design.

Simulations also indicate that higher increases in SNR should be possible if the material permittivity is increased. However, this assumes that the loss tangent remains low relative to the body. For example, conductivities of 0.1, 0.5 and 1.0 S/m result in coil losses of 2.5, 11 and 19% respectively. These simulations show the importance of low-loss HPMs as the gains obtained in Fig. 2(f) are of the same order of magnitude with losses from 0.5 S/m onward, nullifying the HPM's effect.

One of the potential disadvantages of using integrated HPMs is the increase in weight of the array. The three-element integrated HPM coil in this paper has a mass of 760 g, but this was not perceived as uncomfortable by any of the subjects in this study. This is in line with previous studies, where even larger amounts of HPM up to 4 kg on the chest have been used [25]. The use of integrated HPM coils would be much easier to realize in, for example, posterior body arrays integrated into the scanner bed. Weight can possibly be reduced by using water-based ceramics. Although their effectiveness has been shown in literature, their use in fully integrated HPM coils might be limited, as high relative permittivities (>300) are difficult to obtain and conductivities are often higher than 0.1 S/m [2,3,9].

Declaration of Competing Interest

The authors declare that they have no known competing financial interests or personal relationships that could have appeared to influence the work reported in this paper.

Acknowledgements

The authors would like to thank Wyger Brink for performing simulations relating to this work and for extended discussions. This work was funded by the ERC under grant number 670629 and 737180, and by the NWO domain AES under grant number 13375.

Appendix A. Supplementary material

Supplementary data to this article can be found online at https://doi.org/10.1016/j.jmr.2019.106681.

References

[1] Q.X. Yang, W. Mao, J. Wang, M.B. Smith, H. Lei, X. Zhang, K. Ugurbil, W. Chen, Manipulation of image intensity distribution at 7.0 T: passive RF shimming and focusing with dielectric materials. Journal of Magnetic Resonance Imaging: An Official Journal of the International Society for, Magn. Reson. Med. 24 (2006) 197–202.
[2] W.M. Teeuwisse, W.M. Brink, A.G. Webb, Quantitative assessment of the effect of high-permittivity pads in 7 Tesla MRI of the brain, Magn. Reson. Med. 67 (2012) 1285–1293.
[3] W.M. Brink, Dielectric shimming: exploiting dielectric interactions in High Field MRI PhD thesis, Department of Radiology, Leiden University Medical Center, 2016.

[4] G.G. Haemer, G. Carluccio, C.M. Collins, Design of an 8Ch Dipole Transmit Array for Head Imaging with the use of a High Permittivity Material Helmet Shaped Former, in: 2018 International Conference on Electromagnetics in Advanced Applications (ICEAA), IEEE, 2018, pp. 601–604.
[5] A. Manoliu, G. Spinner, M. Wyss, D.A. Ettlin, D. Nanz, F.P. Kuhn, L.M. Gallo, G. Andreisek, Magnetic resonance imaging of the temporomandibular joint at 7.0 T using high-permittivity dielectric pads: a feasibility study, Invest. Radiol. 50 (2015) 843–849.
[6] W.M. Brink, A.M. van der Jagt, M.J. Versluis, B.M. Verbist, A.G. Webb, High permittivity dielectric pads improve high spatial resolution magnetic resonance imaging of the inner ear at 7 T, Invest. Radiol. 49 (2014) 271–277.
[7] G. Carluccio, G. Haemer, M. Vaidya, S. Rupprecht, Q. Yang, C.M. Collins, SNR Evaluation for a high-permittivity dielectric helmet-shaped coil former for a 28 channel receive array, in: Proceedings 26. Annual Meeting International Society for Magnetic Resonance in Medicine, Vol. 26. Paris, France, 2018, pp. 4405.
[8] M.V. Vaidya, C.M. Deniz, C.M. Collins, D.K. Sodickson, R. Lattanzi, Manipulating transmit and receive sensitivities of radiofrequency surface coils using shielded and unshielded high-permittivity materials, Magn. Reson. Mater. Phys., Biol. Med. 31 (2018) 355–366.
[9] Q.X. Yang, J. Wang, J. Wang, C.M. Collins, C. Wang, M.B. Smith, Reducing SAR and enhancing cerebral signal-to-noise ratio with high permittivity padding at 3 T, Magn. Reson. Med. 65 (2011) 358–362.
[10] Z. Yu, X. Xin, C.M. Collins, Potential for high-permittivity materials to reduce local SAR at a pacemaker lead tip during MRI of the head with a body transmit coil at 3 T, Magn. Reson. Med. 78 (2017) 383–386.
[11] C.M. Collins, G. Carluccio, B. Zhang, G. Adriany, K. Ugurbil, R. Lattanzi, On the Relationship Between Field Strength and Permittivity for Desired Effect of High-Permittivity Materials in MRI, in: Proceedings 27. Annual Meeting International Society for Magnetic Resonance in Medicine, Vol. 27. Montreal, Canada, 2019, pp. 1566.
[12] K. Koolstra, P. Börnert, W. Brink, A. Webb, Improved image quality and reduced power deposition in the spine at 3 T using extremely high permittivity materials, Magn. Reson. Med. 79 (2018) 1192–1199.
[13] S. Rupprecht, C.T. Sica, W. Chen, M.T. Lanagan, Q.X. Yang, Improvements of transmit efficiency and receive sensitivity with ultrahigh dielectric constant (uHDC) ceramics at 1.5 T and 3 T, Magnetic Resonance Med. 79 (2018) 2842–2851.
[14] I. Zivkovic, W. Teeuwisse, A. Slobozhanyuk, E. Nenasheva, A. Webb, High permittivity ceramics improve the transmit field and receive efficiency of a commercial extremity coil at 1.5 Tesla, J. Magn. Reson. 299 (2019) 59–65.
[15] M.V. Vaidya, D.K. Sodickson, C.M. Collins, R. Lattanzi, Disentangling the effect of high permittivity materials on signal optimization and sample noise reduction via ideal current patterns, Magn. Reson. Med. 81 (2019) 2746–2758.
[16] O. Ocali, E. Atalar, Ultimate intrinsic signal-to-noise ratio in MRI, Magn. Reson. Med. 39 (1998) 462–473.
[17] D.K. Sodickson, R. Lattanzi, M. Vaidya, G. Chen, D.S. Novikov, C.M. Collins, G.C. Wiggins, The Optimality Principle for MR signal excitation and reception: new physical insights into ideal RF coil design, in: Proceedings 25. Annual Meeting International Society for Magnetic Resonance in Medicine, Vol. 25. Honolulu, Hawaii, 2017, pp. 0756.
[18] H. Fujita, T. Zheng, X. Yang, M.J. Finnerty, S. Handa, RF surface receive array coils: the art of an LC circuit, J. Magn. Reson. Imaging 38 (1) (2013) 12–25.
[19] X. Yan, J.C. Gore, W.A. Grissom, New resonator geometries for ICE decoupling of loop arrays, J. Magn. Reson. 277 (2017) 59–67.
[20] D. Seeber, J. Jevtic, A. Menon, Floating shield current suppression trap, Concepts Mag. Resonance Part B: Mag. Resonance Eng.: Edu. J. 21 (2004) 26–31.
[21] P. Kellman, E.R. McVeigh, Image reconstruction in SNR units: a general method for SNR measurement, Magn. Reson. Med. 54 (2005) 1439–1447.
[22] K. Nehrke, P. Börnert, DREAM|-a novel approach for robust, ultrafast, multislice B1 mapping, Magn. Reson. Med. 68 (2012) 1517–1526.
[23] T. Ruytenberg, B.M. Verbist, J. Vonk-Van Oosten, E. Astreinidou, E.V. Sjögren, A. G. Webb, Improvements in high resolution laryngeal magnetic resonance imaging for preoperative transoral laser microsurgery and radiotherapy considerations in early lesions, Front. Oncol. 8 (2018) 216.
[24] P. De Heer, W.M. Brink, B.J. Kooij, A.G. Webb, Increasing signal homogeneity and image quality in abdominal imaging at 3 T with very high permittivity materials, Magn. Reson. Med. 68 (4) (2012) 1317–1324.
[25] S. Aussenhofer, A. Webb, An eight-channel transmit/receive array of TE01 mode high permittivity ceramic resonators for human imaging at 7 T, J. Magn. Reson. 243 (2014) 122–129.